Finite element simulation of fretting wear-fatigue interaction in spline couplings

J. Ding*, S. B. Leen, E. J. Williams and P. H. Shipway

This paper describes a finite element based method for simulating the effects of material removal, associated with fretting wear, on fretting fatigue parameters in a spline coupling. An incremental wear simulation technique is implemented with a single tooth finite element model of the coupling for symmetric loading, assuming equal wear on all teeth, using a comparatively coarse mesh model, for computational efficiency. A surface interpolation technique is implemented to map the predicted distributions of wear onto a non-symmetric, 360° (18-tooth) model, with detailed refinement on one tooth, to predict the effect of wear on the evolution of stress, strain and fatigue parameters and on subsequent life prediction. The life prediction is based on a critical plane multiaxial fatigue parameter approach, along with cumulative damage for combined load cycles and for wear induced changes in the fatigue parameters. Furthermore, the effect of wear due to the rotating bending moment and fluctuating torque on fretting fatigue damage accumulation is presented. Low frequency, torque and axial loading induced wear, leading to gross slip conditions on all teeth, is predicted to reduce fretting fatigue parameters and hence increase life. In contrast, higher frequency, rotating moment and fluctuating torque induced wear, corresponding to partial slip conditions, is predicted to increase fretting fatigue parameters away from the contact edges and hence lead to fretting fatigue cracking away from the contact edges and, for the case studied here, to a reduction in predicted life, as observed experimentally. The results are interpreted vis-à-vis published test data for scaled aeroengine splines.

Keywords: Fretting fatigue, Fretting wear, Smith–Watson–Topper, Critical plane, Ruiz, Spline couplings

List of symbols

a_1	spline axial direction contact width
a_2	spline tooth flank (involute profile) direction contact width
b	fatigue strength exponent
B	applied bending moment
B_n	design case bending moment
c	fatigue ductility exponent
E	Young's modulus
f	frequency of rotation
F	applied axial load
F_n	design case axial load
h	total wear depth
k	dimensional Archard wear coefficient
m	load increment number
n	wear step number
ΔN	number of increments per load step
$N_{f,n}$	predicted number of combined cycles to failure
$N_{f,n}^{maj}$	number of major cycles to failure without minor cycles acting
$N_{f,n}^{min}$	number of minor cycles to failure without major cycles acting
N_{tooth}	number of teeth in the spline coupling
N_T	experimental measured number of major cycles to failure
p	contact pressure
p_0	mean contact pressure
R_i	radius of node i on the external spline
s	relative slip
t	time
T	applied torque
T_n	design case torque
x	distance from tooth tip along spline profile
X	global X coordinate
Y	global Y coordinate
z	axial distance along the length of the spline tooth
Z	global Z coordinate
δ	relative slip amplitude between two contacting surfaces
δ_n	relative slip between contacting surfaces along the n direction
ε_f'	fatigue ductility coefficient

University Technology Centre in Gas Turbine Transmission Systems, School of Mechanical, Materials and Manufacturing Engineering, University of Nottingham, Nottingham, NG7 2RD, UK

*Corresponding author, email jian.ding@nottingham.ac.uk

Received 12 December 2007; accepted 7 May 2008
DOI 10.1179/175158308X320791

ε_y measured monotonic failure (true) strain
θ angle between node i and X direction
σ_{max} maximum normal stress on the critical plane
σ_y yield stress (0·1% proof stress of material)
σ_f' fatigue strength coefficient
τ contact surface shear traction
ω accumulate damage
$\Delta\varepsilon_a$ maximum normal strain amplitude

Introduction

Fretting, that is, small amplitude oscillatory displacement between surfaces in contact, is a phenomenon observed in many mechanical assemblies and can significantly reduce the life of an assembly. Depending on the imposed forces and relative displacements, the resulting damage may be wear (material removal), fatigue (cracking) or both. Since the 1950s, many studies have been carried out on fretting fatigue and fretting wear for various contact geometries and material combinations. However, few have quantitatively investigated and characterised the transition, competition and interaction between fretting wear and fretting fatigue. Vingsbo and Soderberg[1] developed a 'fretting map' approach that qualitatively maps how fretting damage evolution depends on slip amplitude, and indicates that the risk of both fretting wear and fatigue in the partial slip regime increases with increasing slip amplitude, whereas, for the gross slip regime, fatigue damage is reduced significantly even though wear continues to increase with increasing slip amplitude. So far, these phenomena are still not clearly explained, in particular, from a quantitative point of view.

In the literature fretting fatigue and fretting wear are most often studied separately according to the requirements of varying applications. Extensive studies have been carried out on the prediction of fretting fatigue by making use of initial contact geometries and ignoring their evolution with fretting wear. Several researchers[2–4] suggest that although the stress distribution near the fretting surface is complex owing to contact pressure and cyclic shear traction combined with cyclic bulk fatigue stresses, fretting fatigue is still basically a multiaxial fatigue phenomenon. Thus, fretting fatigue lives are commonly predicted using conventional multiaxial plain fatigue parameters, for example, the Smith–Watson–Topper (SWT) and Fatemi–Socie (FS) parameters. Analytical and numerical implementations of the critical plane SWT and FS can produce reasonable predictions of fretting fatigue life under partial slip conditions for commonly used (simple) laboratory fretting geometries.[2–5] However, it is important to point out that satisfactory accuracy for these approaches is generally limited to the small slip ranges where the imposed relative displacement is mainly accommodated by elastic deformation of the contact, and wear and oxidation from the slip zone are small. With increasing slip, the damage process associated with fretting contact will be a synergistic competition between wear, corrosion and fatigue phenomena. As a result, stress/strain based lifing methods consistently fail to predict the effect of slip on fretting fatigue, e.g. Jin and Mall.[6] The Ruiz parameters[7] are an empirical approach which account for slip, but their application is generally considered to be limited to predicting crack location, as opposed to cycles to failure (fatigue life).

Fretting wear is typically more gradual and progressive, compared with fretting fatigue; however, it can still significantly add to the maintenance cost of a component subjected to fretting. A number of efforts have been made to computationally simulate fretting wear. McColl *et al.*[8] and Ding *et al.*[9] recently reported an automated fretting wear simulation tool based on finite element (FE) implementation of a modified Archard wear equation. The results showed that wear patterns are significantly different in partial slip and gross slip situations. As the contact geometry evolves, an important and interesting finding is that partial slip wear leads to an increase in the salient fatigue stress and strain components at the stick slip interface whereas gross slip wear ameliorates the same stresses. More recently, Madge *et al.*[10,11] combined the above mentioned wear modelling technique with a multiaxial SWT based damage accumulation approach to predict fretting fatigue with evolving fretting contact conditions. The approach was employed to explain experimental results as reported by Jin and Mall,[6] for a Hertzian contact configuration.[11] The results show the capability of the combined use of wear and fatigue damage accumulation to capture complex phenomenon for comparatively simple fretting contacts. The same approach has also been successfully applied to a rounded punch on flat fretting arrangement to predict the measured effect of relative slip on fretting fatigue life.[10] This work established the importance of simulating wear induced material removal, leading to changes in contact surface profiles and associated redistribution of surface and subsurface stresses, for fretting fatigue life prediction. Specifically, high slip amplitudes at the gross slip regime widen the contact patch and correspondingly level off the maximum fatigue damage accumulation within the contact, leading in general to an increase in fatigue life in the gross slip regime. In contrast, in the partial slip regime, the location of maximum damage accumulation starts off near the edge of contact for small numbers of cycles; as the wear damage accumulates, the critical location moves steadily towards the stick/slip interfaces.

This paper is concerned with the development of an integrated modelling approach for fretting wear and fretting fatigue in a complex three-dimensional (3D) assembly, i.e. a reduced scale aeroengine type spline coupling. The application is to the type of couplings employed in gas turbine aeroengines to connect the low pressure turbine and compressor shafts, for which a scientific design methodology requires consideration of surface damage failure modes (e.g. wear and fretting) as well as plain fatigue. These couplings are designed principally for torque and axial load transmission and experience wide variations in torque between takeoff, cruise and landing conditions. However, they are also subjected to rotating bending moments due to gyroscopic effects during flight manoeuvres and engine carcass deformations. Small scale spline tests, where the specimens had the representative tooth dimensions, contact loads and stresses of full size aeroengine splines, have previously been conducted at the University of Nottingham to improve the understanding of failure behaviour under these complex in-service loading conditions.[12] Quantitative analyses of fretting wear and fretting fatigue from spline tests have also been reported separately. It was found that FE implementation of a

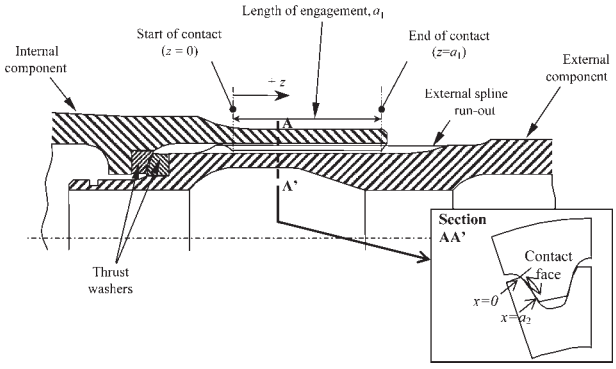

1 Schematic half section of splined coupling geometry showing important features, and *x* and *z* coordinates

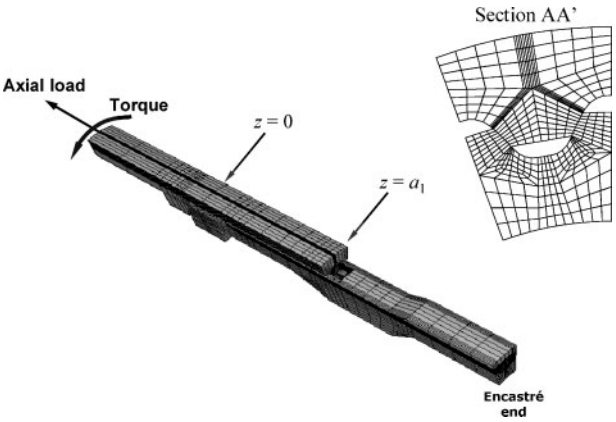

2 One tooth cyclic symmetry FE model of spline coupling, using coarse mesh for efficient wear simulation predictions

critical plane multiaxial fatigue parameter SWT, along with the localised mesh refinement technique employed to capture the multiaxial contact stress distributions, is successful in predicting the general trend of increasing fretting fatigue damage, and hence reducing life, with increasing bending moment.[13] However, the approach was shown to have shortcomings with respect to prediction of failure location. This was attributed, at least partly, to the predictions being based on the initial geometry, i.e. ignoring contact geometry evolution with fretting wear. Such wear could be expected to affect stress, strain and fatigue damage distributions within the contact regions and thus the predicted locations of fretting crack initiation. The work presented here addresses this issue by using an incremental technique to simulate material removal, combined with FE implementation of the critical plane SWT parameter and using fatigue damage accumulation, to assess the effect of fretting wear on fretting fatigue damage accumulation. A key challenge here is to find a compromise between the detailed mesh refinement required for sufficiently accurate resolution of stresses, strains and hence fatigue damage variables (e.g. SWT) and the need for a low node count for the computationally intensive incremental wear modelling.

Spline geometry, loading and material

A small scale spline testing facility has been built in the University of Nottingham to improve the understanding of fatigue behaviour under such complex inservice loading conditions. The specimens are manufactured from a high strength Cr–Mo–V steel using the manufacturing route employed for service aeroengine shafts. They have 18 teeth on a reduced diameter, but retain the representative tooth dimensions of real aeroengine splines. Figure 1 shows the spline geometry, together with definition of the contact axial length coordinate z, the tooth flank contact width coordinate x and the maximum possible contact dimensions a_1 and a_2. More detailed information has been presented elsewhere.[12]

An important feature of the spline couplings studied here is the barrelled profile on the external spline. Barrelling refers to axial variations of the thickness of the external spline teeth to create a more uniform axial contact pressure distribution and, in particular, to reduce end of contact stress peaks. As a result, the new external tooth will no longer conform nominally to the profile of the internal spline tooth, which introduces an additional complexity into spline design. In particular, the spline contact is neither Hertzian nor punch on flat, but is inherently 3D with a complex 3D contact patch, e.g. Ref. 13. Consequently, this makes the wear-fatigue interaction and modelling of it significantly more complex than Hertzian or punch on flat fretting geometries, as studied by Madge *et al.*[10,11]

The fatigue tests conducted simulate the key life limiting loading experienced by the splines during a typical civil flight envelope consisting of the combined major and minor cycle loading sequence. Each major cycle involves the application of a mean torque T_{MEAN} and axial load that are ramped up over a 4 s period and then held constant while 500 minor cycles are superimposed. Each minor cycle consists of a sinusoidal torque fluctuation ($\pm 5\%$ T_{MEAN}) and a rotating bending moment of constant magnitude, applied in-phase at a frequency of 5 Hz. The non-dimensionalised design torque T_{n}, axial load F_{n} and bending moment B_{n}, values for the coupling are 0·818, 0·032 and 0·039 respectively, where T_{n}, F_{n} and B_{n} are defined as follows

$$T_{\mathrm{n}} = \frac{T}{T^{\mathrm{m}}_{\mathrm{yp}}} \quad F_{\mathrm{n}} = \frac{F}{F^{\mathrm{m}}_{\mathrm{yp}}} \quad B_{\mathrm{n}} = \frac{B}{B^{\mathrm{m}}_{\mathrm{yp}}} \tag{1}$$

with T, F, B as torque, axial and bending load respectively. $T^{\mathrm{m}}_{\mathrm{yp}}$, $F^{\mathrm{m}}_{\mathrm{yp}}$, $B^{\mathrm{m}}_{\mathrm{yp}}$ are the maximum elastic torque, axial load and bending capacities for a shaft with outer diameter equal to the minor diameter of the externally splined shaft and inner diameter equal to $0{\cdot}52 \times$ pitch circle diameter of the externally splined shaft respectively. The calculations of $T^{\mathrm{m}}_{\mathrm{yp}}$, $F^{\mathrm{m}}_{\mathrm{yp}}$, $B^{\mathrm{m}}_{\mathrm{yp}}$ are based on the yield stress (0·1% proof stress) of the spline material σ_{y}.

The details of spline test results in terms of wear measurements[14] and fatigue cracking behaviour[12] have been reported on previously. These are further discussed below in the 'Discussion' section, in the context of the wear fatigue predictions.

Finite element modelling of spline coupling

Previous studies, e.g. Ref. 12, have shown that a one tooth, cyclic symmetry FE model simulating one 20° segment of the coupling, as shown in Fig. 2, can be used for cyclically symmetric loading conditions, such as torque and axial load. This simplification has previously

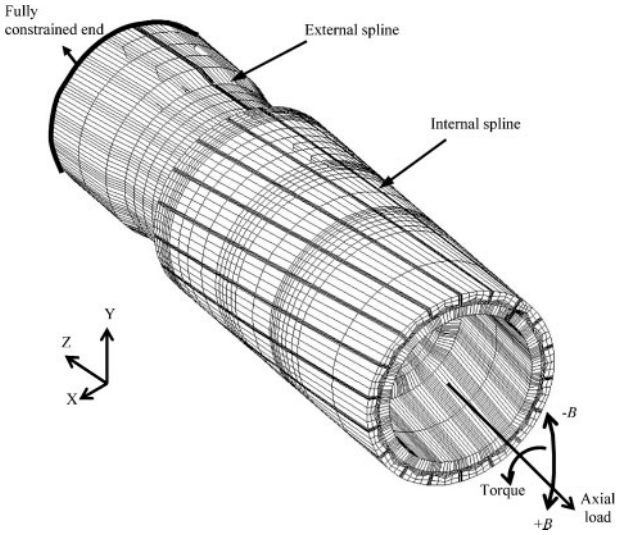

3 Full 360° (18-tooth) FE model of spline coupling showing constraints on external spline and loads applied to internal spline

facilitated a high level of mesh refinement and thus detailed stress, strain and contact variable results, so that the fatigue behaviour of the coupling under the major cycle loading can be accurately captured. However, with the introduction of non-symmetric loading, i.e. rotating bending moment with in-phase fluctuating torque, it becomes necessary to model the full 18-tooth 360° geometry. The need for accurate stress and strain predictions would significantly increase the demand on mesh refinement at the cost of computational resources. A localised mesh refinement technique using multipoint constraints has therefore been developed.[15] The full FE model is shown in Fig. 3 with eight node linear brick elements being used throughout. Figure 4 shows a cross-section of the external spline model showing the tooth numbering convention used and the level of mesh refinement, especially on the top dead centre tooth (i.e. tooth 18). It can be seen that this approach has permitted the use of a fine FE mesh on tooth 18 with a very much coarser mesh on all other teeth. The measured elastic-plastic properties for the material are given in Ref. 12; an isotropic, von Mises hardening model with a multilinear curve was employed. Negligible plastic deformation is predicted to occur for the range of load cases analysed here.

In the FE model, torque, bending moment B and axial loads are applied at the rear end of the internal spline in the direction of the arrows of Fig. 3. Also the torque fluctuates between T_{max} (105% T_{mean}) and T_{min} (95% T_{mean}) during the minor cycle loading. The bending moments $+B$ and $-B$, correspond respectively to the maximum and minimum total torque values T_{max} and T_{min}. The bending moment is applied at a constant magnitude about a transverse axis, which rotates around the axis of the shaft. This is implemented via two bending components B_1 and B_2, which are 90° out of phase with one another. Referring to Fig. 5*a*, with B as the total bending moment, t as the time increment and f as the frequency of rotation, B_1 and B_2 are defined respectively by

$$B_1 = -B\sin(2\pi ft) \tag{2}$$

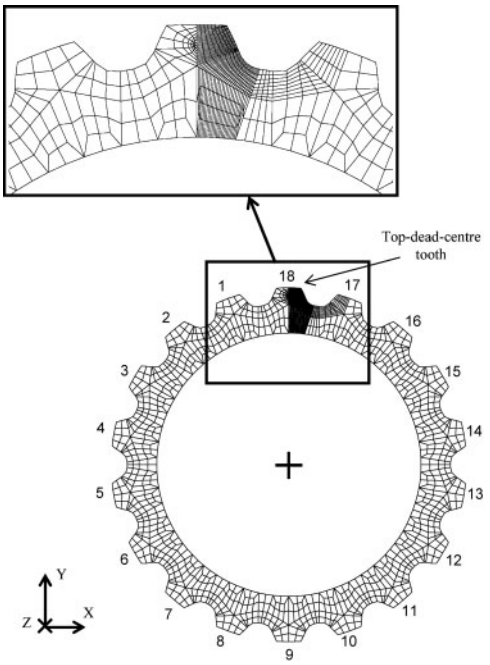

a FE implementation of constant magnitude rotating bending moment; *b* applied loading sequence

4 Cross-section through 360° (18-tooth) FE model of external spline showing tooth numbering scheme and localised mesh refinement on tooth 18 (*z* axis directed out of page)

$$B_2 = B\cos(2\pi ft) \tag{3}$$

Figure 5*b* shows the load sequence of the FE model, which consists of six steps and simulates one major cycle loading followed by as many minor cycles as required to give a stable cycle:

(i) step 1: major cycle torque $T_{mean}=0{\cdot}779\ T_{yp}^{m}$ and axial load $F_d=0{\cdot}032\ F_{yp}^{m}$ are applied by ramping up linearly from zero to their respective values. Axial load is held constant hereafter

(ii) step 2: minor cycle bending load, $+B$ is applied, by ramping up the B_2 component from zero to B, together with the maximum total torque T_{max}, which is ramped up linearly from the major cycle torque

(iii) step 3: bending load is rotated from $+B$ to $-B$ by varying B_1 and B_2 components. B_1 is varied according to a sine curve from zero to $-B$ and back to zero, while B_2 is varied according to a cosine curve from $+B$ to zero to $-B$. At the same time, the total torque is varied linearly from T_{max} to T_{min}, which is the minimum total torque

(iv) step 4: bending load is rotated from $-B$ to $+B$. B_1 is varied according to a sine curve from zero to $+B$ and back to zero; while B_2 is varied according to a cosine curve from $-B$ to zero to $+B$. At the same time, the total torque is varied from T_{min} to T_{max}, the maximum total torque

(v) steps 5 to 10: same as steps 3 to 4.

Studies have shown that six load steps (two complete minor cycles) are sufficient to capture the steady state behaviour of stresses, strains and slips during the minor cycle loading. Based on the loading sequence above, it can be seen that tooth 18 (top dead centre tooth),

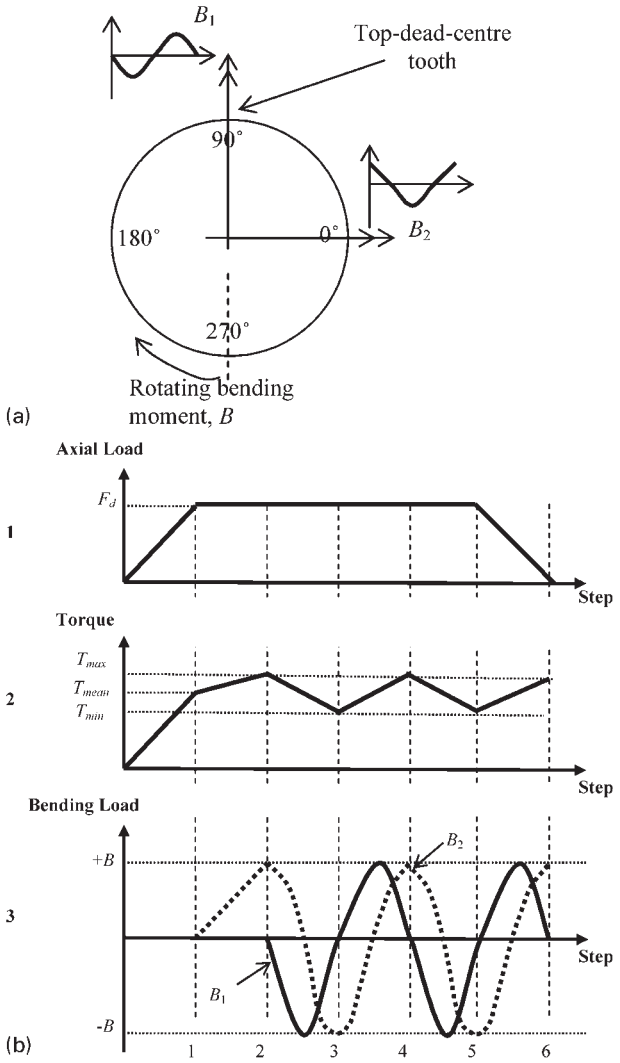

5 Schematic diagram of loading sequence applied to 360° (18-tooth) FE model in order to simulate experimental loading regime

experiences maximum tensile stresses from the rotating bending moment ($+B$), at the same time that it experiences the maximum total torque, $T_{\max}$ (step 4 or 6). This condition will be referred to as the maximum minor load. The minimum minor load condition for this tooth is during step 3 where $-B$ and $T_{\min}$ occur simultaneously.

In this study, the basic Coulomb friction model with isotropic friction is employed within the contact regions. Frictional contact conditions are determined via the penalty method with an allowable elastic slip of $\delta/a_2 = 2{\cdot}8 \times 10^{-5}$. Based on cylinder on flat tests for a representative range of loads and strokes,[16] a coefficient of friction (COF) of 0·3 is assumed as a representative average value over 100 000 cycles.

Combined wear fatigue lifing methodology

Modelling of wear

Modelling of material removal due to wear is essential for the required integrated fretting wear-fatigue methodology, for it predicts not only the extent of wear damage, but also the concomitant change in fatigue-pertinent stresses and strains. A modified form of Archard's equation[8,17] is used here to predict the local wear depth increment for a given point within the contact

$$\mathrm{d}h = kp\,\mathrm{d}s \tag{4}$$

where h is the wear depth (mm), k is the dimensional wear coefficient defined as the wear per unit slip per unit contact pressure, p is the contact pressure and s is contact slip.

Ding[16] has developed a computer programme to implement this equation incrementally in parallel with the ABAQUS FE code and the results of this implementation have been validated against cylinder-on-flat fretting wear tests for the spline material combination employed here over a range of stroke and load combinations.[8] More recent work by Madge *et al.*[11] has implemented equation (4) via an adaptive meshing user subroutine called UMESHMOTION, within ABAQUS; in this case, the application was to the prediction of fretting fatigue life of titanium fretting fatigue specimens. The user subroutine implementation is more accurate and efficient than that of Ref. 8 in the following aspects:

(i) the spatial adjustment of the contact nodes is now achieved within an adaptive meshing framework

(ii) one implication of this is that, whereas previously the wear depth was calculated using the contact pressure for normal loading only and with an average relative slip over the tangential load cycle,[8] now the incremental wear depth is calculated for each increment of the tangential load cycle (fretting cycle) using the associated instantaneous values of contact pressure and relative slip

(iii) whereas previously a separate analysis was needed for each cycle jump, with an attendant unloading and reloading of the normal load, the new implementation circumvents this, since the geometry modification is effected within the FE code itself. This is more consistent with the actual experimental situation

(iv) small cycle jumps give finer discretisation of the time domain helping to maintain stability and accuracy; larger jumps decrease the computational expense. Since the present implementation modifies the geometry incrementally throughout the tangential cycle, it is more stable and hence much larger cycle jumps can be made.

However, one disadvantage of the user subroutine approach is that all of the fretting cycle wear incrementation data now need to be stored in memory while the single analysis is running. This leads to limitations to the model size and incrementation discretisation, which in some cases, can become prohibitive.

The user subroutine approach is implemented here for the cylinder on flat fretting wear geometry of Fig. 6*a* for the high strength steel, as employed in the spline coupling. The two-dimensional (2D) FE model of Fig 6*b* is employed for the analysis and other details of the FE model and fretting tests are available in Ref. 8. A wear coefficient of $5{\cdot}0 \times 10^{-8}$ MPa^{-1}, which is representative of the high strength steel up to 18 000 fretting

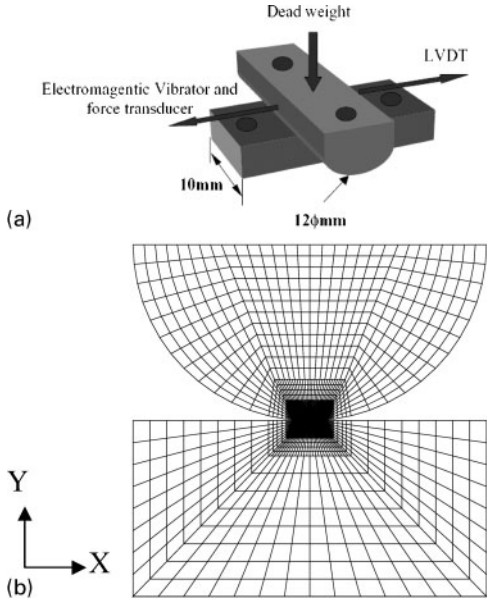

6 *a* schematic of cylinder on flat fretting wear test geometry and *b* 2D FE contact model for wear simulation

Table 1 Parameters for cylinder on flat fretting cases studied

Case no.	Normal load, N mm^{-1}	Peak to peak slip amplitude, μm
1	120	±10
2	120	±2·5

wear cycles,[8] is employed. Two load cases are studied; a partial slip case and a gross slip case, as listed in Table 1. Figure 7*a* and *b* shows a comparison between the user subroutine approach to wear simulation and the previous approach of Ref. 8 (which operates external to the FE code) in terms of the predicted contact geometry evolutions up to 10 000 cycles. Note that only the worn geometries are plotted for the user subroutine approach. Clearly, the results of the two methods are indistinguishable. From the point of view of application to the complex spline coupling wear simulation, the user subroutine is preferable.

The wear modelling approach of Ding[16] has been previously applied[18] to the spline problem. The same approach is employed here, but the implementation is

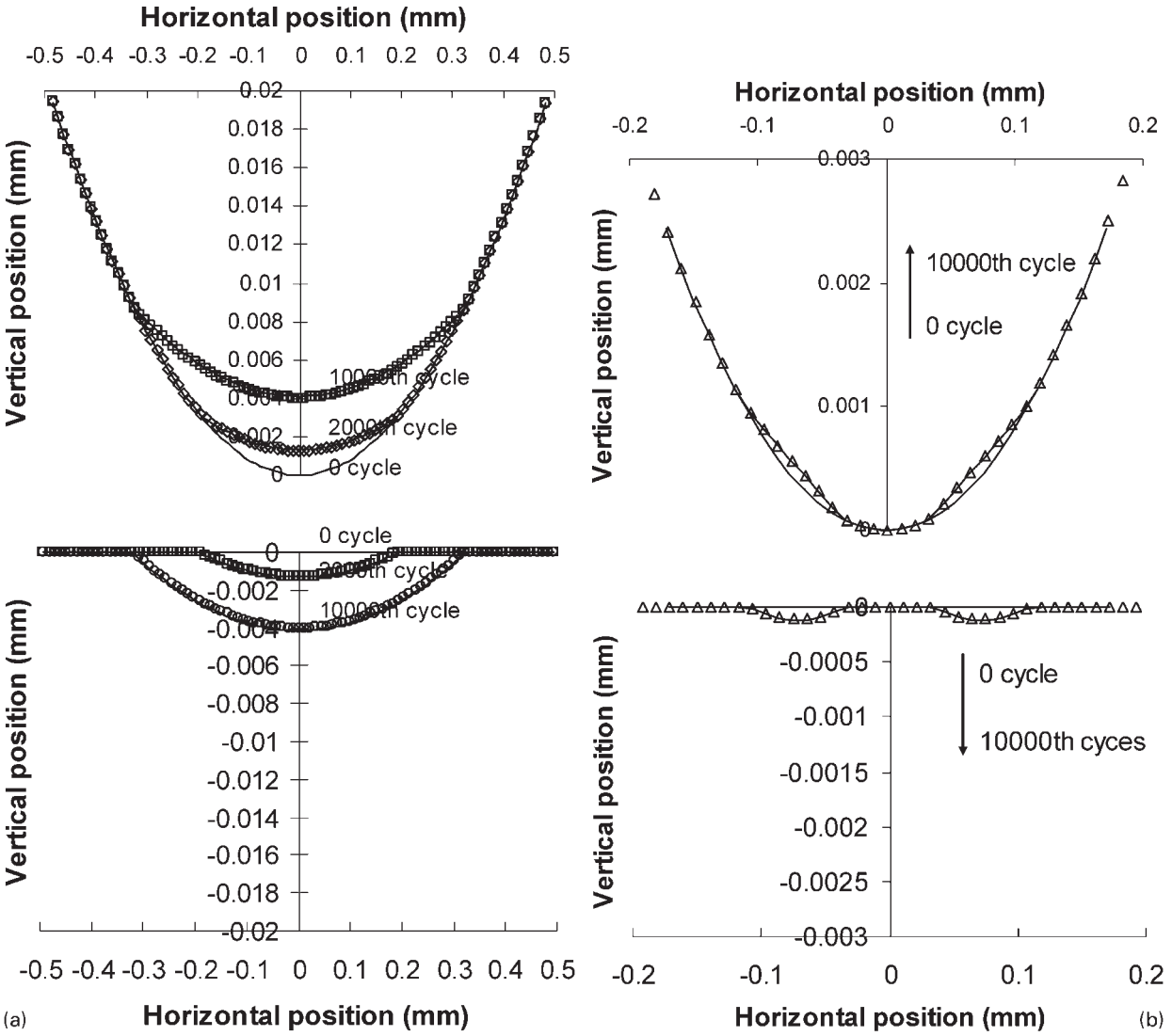

7 Comparison of predicted evolution of contact surface profiles obtained from two fretting wear modelling approaches for *a* gross slip and *b* partial slip conditions: solid lines represent worn surface profiles obtained from method 1; symbols represent worn surface profiles obtained from method 2

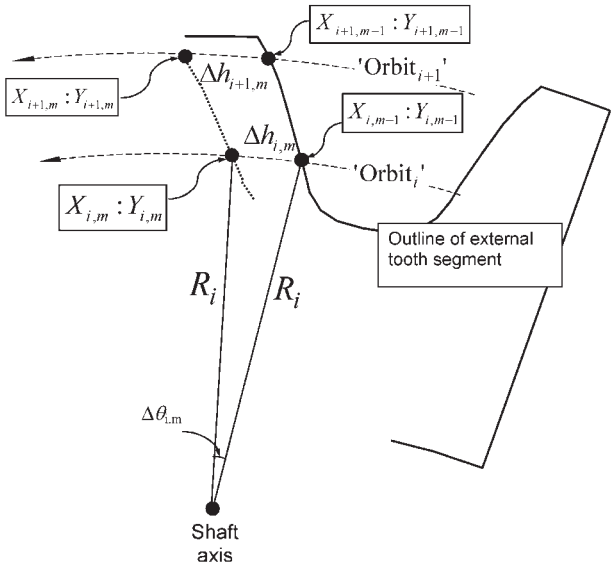

8 Schematic transverse section through external tooth segment showing movement of contact nodes in response to step *n* and displacement required to return node *i* to its 'orbit' after this step: *X* and *Y* are global coordinates (not to scale)

within UMESHMOTION. A cycle jumping technique is employed whereby the required total number of wear cycles N_T is achieved by n wear blocks, each corresponding to a block of ΔN wear cycles. The feasible values of ΔN are determined by the stability of the subsequent contact pressure and slip calculations. Generally, as the pressure variation across the contact diminishes, higher values of ΔN can be tolerated. For each block of ΔN wear cycles, the normal and tangential loading cycle is applied incrementally for $m=1$ to m_{inc}. A value of $m_{inc}=20$ is used here. Following equation (4), the wear depth increment $\Delta h_{i,m}$ at each contact node i for the mth load increment is calculated by

$$\Delta h_{i,m} = k\Delta N p_i \Delta s_i = k\Delta N p_{i,m} \Delta s_{i,m} \quad (5)$$

where $p_{i,m}$ is the contact pressure and $\Delta s_{i,m}$ the (resultant) slip increment at contact node i for increment m.

Equation (5) provides the magnitude of the wear increment $\Delta h_{i,m}$ for each nodal position, but not the direction. To obtain this, the directions of the local slip and contact pressure are required. ABAQUS computes the local slip components in the local slip plane, which is transverse to the local outwards surface normal. The local contact pressure is also in the direction of the local outwards surface normal. Thus at each 'worn node', the wear depth should be proportional to the product of the local resultant in-plane slip and the component of the contact pressure normal to the slip plane. As a result, 'worn nodes' will be moved off their original circumferential orbits when the wear depth increments are applied (Fig. 8). To avoid a loss of cyclic symmetry, the wear direction in this study is assumed to be tangential to the original 'orbits'. The geometrical implementation is illustrated in Fig. 8, which shows two contact nodes (i and $i+1$) on a transverse section through an external tooth segment after increments $m-1$ and m. From Fig. 8 it can be readily shown that

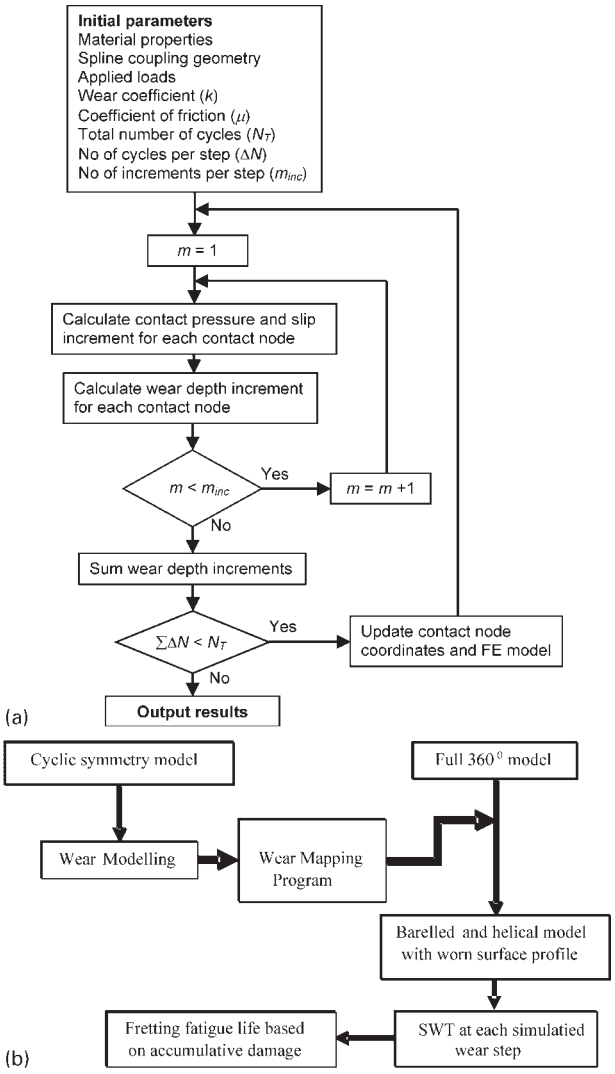

9 *a* flowchart for wear simulation of spline coupling and *b* analysis procedure for critical plane fatigue damage parameter SWT with evolving contact geometry

$$X_{i,m} = R_i \cos(\theta_{i,m-1} - \Delta\theta_{i,m}) \quad (6)$$

$$Y_{i,m} = R_i \sin(\theta_{i,m-1} - \Delta\theta_{i,m}) \quad (7)$$

where $\theta_{i,m-1}$ is equal to $\tan^{-1}\left(X_{i,m-1}, Y_{i,m-1}\right)$ and $\Delta\theta_{i,m}$ is equal to $\Delta h_{i,m}/R_i$. The above sequence is repeated until the required total number of wear cycles N_T is reached. The simulation of incremental wear in an FE model of a complex geometry like that of the spline is however a computationally intensive process, with typical simulations taking one and half days for $\sim$12 000 wear cycles on a typical personal computer. The procedure employed here is presented in Fig. 9*a*.

Fatigue life prediction with wear effects

Following the method developed in Refs. 10 and 11, which studied wear-fatigue interaction in 2D fretting fatigue test geometries, where the evolution of the stress–strain histories was simulated for each wear step, a linear damage accumulation law (i.e. Miner's rule)[19] is employed here to accumulate incremental fatigue damage (due to the wear induced variation of stress and strain from one fretting cycle to the next) at each

material point, to predict total life. Fretting fatigue failure at a material point is therefore defined to correspond to the total accumulated damage ω reaching a value of 1, where ω was defined as

$$\omega = \sum_{n=1}^{n=\frac{N_T}{\Delta N}} \frac{1}{N_{f,n}} \tag{8}$$

where $N_{f,n}$ is the number of combined (major minor) cycles to failure for the stress–strain state predicted to correspond to wear step n, calculated using a critical plane implementation of the SWT equation as follows

$$\sigma_{max}\Delta\varepsilon_a = \frac{(\sigma_f')^2}{E}(2N_f)^{2b} + \sigma_f'\varepsilon_f'(2N_f)^{b+c} \tag{9}$$

where σ_{max} is the maximum normal stress on the critical plane, $\Delta\varepsilon_a$ is the maximum normal strain amplitude on the same plane, σ_f' and b are the fatigue strength coefficient and exponent, ε_f' and c are the fatigue ductility coefficient and exponent, E is Young's modulus and N_f is the number of cycles to failure. The SWT approach is based on physical observations that fatigue cracks initiate and grow within a material on certain planes, where the growth and orientation depends on the normal stresses and strains on these planes. A detailed procedure to determine the critical plane and the associated value of SWT can be found in Ref. 5, wherein it was shown that the critical plane SWT approach predictions gave good correlation with measured plain fatigue lives for the present spline coupling. The material constants used for life prediction are given in Table 2.

Corresponding to a given wear step n, the number of combined cycles $N_{f,n}$ to failure is also predicted using Miner's rule. With 500 minor cycles per major cycle, it can be expressed as

$$\frac{1}{N_{f,n}} = \frac{1}{N_{f,n}^{maj}} + \frac{500}{N_{f,n}^{min}} \tag{10}$$

The major and minor cycle lives $N_{f,n}^{maj}$ and $N_{f,n}^{min}$, are determined using the critical plane SWT values for the major and minor cycle load cycles, respectively. Equations (8)–(10) can thus be employed to predict the number of cycles to failure (ω=1).

Accurate wear and fatigue prediction for any geometry using an FE approach requires as fine a mesh as possible, although compromise is always required between required resolution/accuracy of predicted variables and run time. Most analysis of fretting employs comparatively simple geometries and, hence, models. However, the requirement of simulating wear-fatigue in the spline contact introduces a number of complicating and competing factors as follows:

(i) given the use of equation (5) for geometry modification, relatively smooth predicted distributions of contact pressure and slip are desirable for accuracy and resolution, particularly for partial slip situations where mixed stick and slip regions occur and for cases where the contact geometry can change to become discontinuous

(ii) incremental simulation of material removal requires a large number of non-linear (frictional contact) increments, particularly for accurate resolution of tangential loading effects where transitions from stick to slip and vice versa can occur

(iii) for accurate resolution of stresses, strains and fatigue parameters, within contact problems, with discontinuities in contact geometry, e.g. end of engagement, stick-slip interfaces, barrelling, a fine mesh is required, both at and below the surface

(iv) for cyclically symmetric loading, a one tooth model is sufficient, whereas for non-symmetric loading, a 360° model is required, with a fine mesh in the regions of interest, e.g. where significant changes in key fretting variables occur

(v) the geometrical complexities of the spline coupling itself, by definition, result in a large number of elements and nodes

(vi) the complexities of the spline loading cycle, including frictional contact and plasticity effects, as well as the combined (major and minor) loading cycles, require a number of cycles, each with multiple increments, to ensure convergence.

Table 2 Fatigue constants employed for high strength Cr–Mo–V steel*

σ_f'/σ_{ys}	b	$\varepsilon_f'/\varepsilon_y$	c
0·7873 (LCF)	−0·0524 (LCF)	47·2	−0·5
0·7159 (HCF)	−0·0343 (HCF)		

*LCF and HCF are delimited by the SWT uniaxial test values corresponding to $N_f=10^4$.

The 18-tooth 360° model of Fig. 3 consists of ~150 000 elements, where a typical element dimension at the local mesh refinement region is about $0{\cdot}028a_2$ in the x direction. Given the fact that it takes approximately six days for each FE analysis of the 360° model to completely simulate the entire loading sequence on a Pentium 4 dual processor CPU (3·0 GHz) with 2 GB memory, it is not feasible from a run time perspective (not to mention the disk space requirements) to use this model to simulate the wear resulting from, say, 12 000 cycles, with ΔN=500 cycles, at most. Hence, to achieve an acceptable computational overhead for wear simulation, a significantly coarser mesh is required. In the one tooth coarse mesh spline model, as illustrated in Fig. 2, the average element dimension immediately below the contact region is $\sim 0{\cdot}22a_2$ in the x direction and $0{\cdot}55a_2$–$1{\cdot}11a_2$ in the z direction. This is satisfactory from a wear simulation perspective but not from a fatigue life prediction perspective. Hence, a combined use of the cyclic symmetry model and the 360° model for the wear fatigue predictions is implemented here as depicted in the flowchart of Fig. 9*b*. However, there are a number of implications that follow from this:

(i) the incremental wear simulation is limited to the one tooth model. This is predicated on cyclic symmetry and therefore equal wear is assumed on all teeth, so that only major cycle wear, i.e. due to torque and axial load, is modelled incrementally

(ii) the difference in mesh requirements for fatigue and wear analysis requires a technique to transfer the wear patterns obtained from the coarse mesh to the fine mesh model, to allow higher resolution

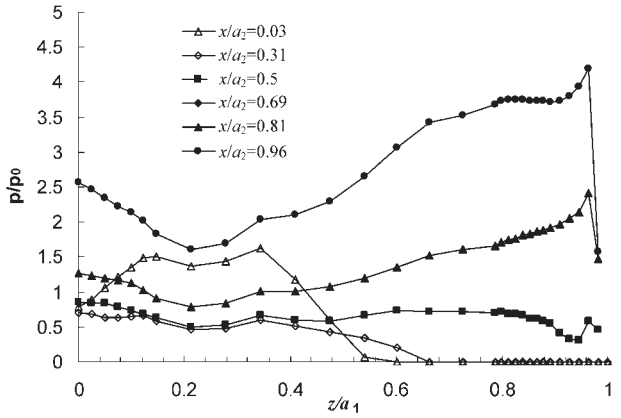

10 Contact pressure distributions versus axial position on TDC tooth of 360° model at maximum minor cycle load for B_n=0·117

damage accumulation with evolving contact geometry to be predicted.

In lieu of an incremental wear simulation for the 360° model, a 'Kriging' surface interpolation approach[20] is used to investigate wear effects. The 'Kriging' method belongs to the family of linear least squares estimation algorithms, which aims to estimate the value of an unknown real function f at a point A^*, given the values of the function at some other points A_1, …, A_n. A Kriging estimator value f(A^*) is a linear combination that may be written as

$$f(A^*) = \sum_{i=1}^{n} \lambda_i f(A_i) \tag{11}$$

The weights λ_i are solutions of a system of linear equations which are obtained by assuming that f is a sample path of a random process F(A^*), and that the prediction error

$$\text{error}(A^*) = F(A^*) - \sum_{i=1}^{n} \lambda_i f(A_i) \tag{12}$$

is to be minimised. A key benefit of this approach for this application is that data can be interpolated from a non-regularly spaced grid distribution of nodes. Hence, by applying the Kriging interpolation approach to the predicted wear depth distribution from the cyclic symmetry model, the surface distribution of wear depth, for each wear step n (n=1, $\frac{N_T}{\Delta N}$), can be obtained for the 18 teeth on the 360° model, with their various degrees of mesh refinement. The overall wear life interaction procedure is depicted in the flowchart of Fig. 9*b*.

Results and discussion

No wear predictions

These (unworn) results have been previously presented elsewhere,[13] but are re-presented here for comparison purposes with the wear results. Figure 10 shows FE predicted contact pressure distributions versus axial position (z/a_1) for different tooth flank (x/a_2) positions on the initial unworn geometry for the design major cycle loading (T_{MEAN}=0·779 T_{yp}^m, F=0·032 F_{yp}^m) with overload minor cycle load (B_n=0·117), as obtained from the 360° model, TDC tooth. The load refers to the maximum minor load, which gives the maximum pressure values during major minor loading sequence. The contact pressure is non-dimensionalised via a mean contact pressure p_0, calculated by assuming the applied torque per tooth to have its centre of action at the pitch circle diameter and dividing the associated force value by the nominal tooth contact area

$$p_0 = \frac{T\cos\beta_p}{N r_p a_1 a_2} \tag{13}$$

where N is the number of spline teeth, r_p is the pitch circle radius, $a_1/\cos\beta_p$ is the helical (nominal) contact length, a_2 is the tooth flank (nominal) contact width and T is the applied torque. The result shows that the contact pressure distributions are complex. Although the pressure distributions versus axial position are not entirely uniform, the barrelling effectively eliminates contact pressure peaks at the z=0 and $z=a_1$ ends of engagement for most tooth flank x positions. One exception is near the tooth flank contact end (x=0·96a_2), where a pressure peak is predicted close to the $z=a_1$ contact end.

Figure 11 summarises the slip features across and along the tooth flanks during the major and minor cycles. The major cycle (step 1) loads cause slipping wherever tooth contact is predicted for the COF of 0·3. However, even with the design major cycle loads fully applied, an appreciable region of potential tooth contact at the high torque end ($z=a_1$) of the external spline remains open. When the minor cycle loads are added,

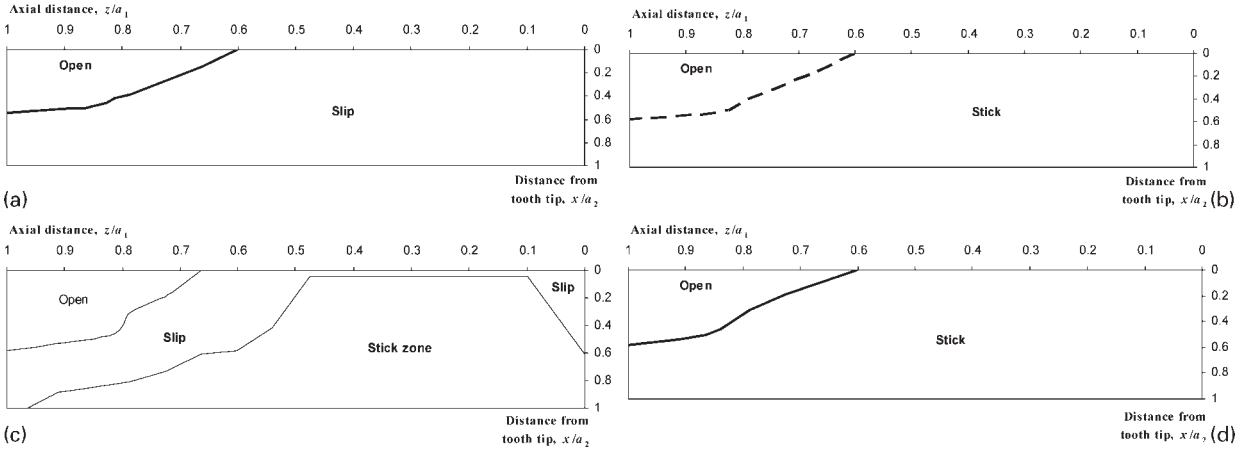

11 Variation of instantaneous contact status for B_n=0·117 case at *a* major load, *b* +*B* and T_{max}, *c* 90 or 270° *B* and T_{mean} and *d* –*B* and T_{min}

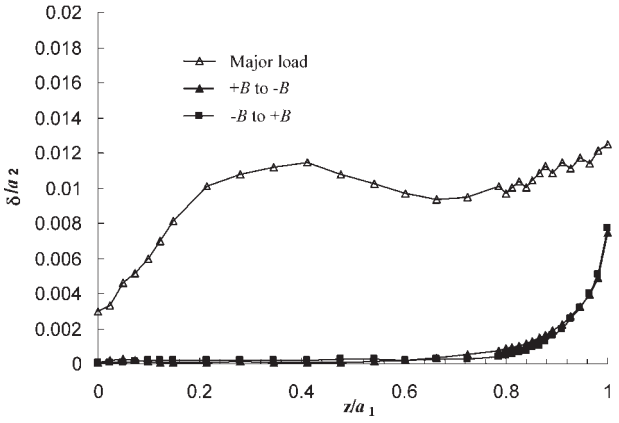

12 Stabilised resultant slip distributions versus axial position at $x/a_2=0{\cdot}96$ tooth flank position for major and minor cycle load of $B_n=0{\cdot}117$ case

the contact status is strongly dependent on the instantaneous orientation of resultant rotating bending moment. The tooth contact remains essentially stuck for the $+B$ or $-B$ bending moment conditions (i.e. $2\pi ft=0$ or $l\pi$, where l is an integer), except for the open region. As the bending moment rotates (steps 2 to 6), a slip zone is introduced that expands and contracts alternately. This slip zone has a maximum size with the bending moment at 90 or 270° orientations as illustrated in Fig. 11*c*. Detailed total (resultant) slip distributions versus axial position at a sample tooth flank location ($x=0{\cdot}96a_2$) are given in Fig. 12. It is clearly seen that gross slip dominates during the major cycle loading, while the application of minor cycle rotating bending moments (either $+B$ to $-B$ or $-B$ to $+B$) results in a mixed stick slip region: the slip is near or at zero (i.e. stick) between $z=0$ to $z=0{\cdot}6a_1$ but increases significantly and monotonically from $z\approx 0{\cdot}7a_1$ to $z=a_1$.

The effect of bending magnitude on the above two contact variables is illustrated in Fig. 13. Figure 13*a* shows that the contact pressure on tooth 18 decreases uniformly with decreasing bending magnitude at the $x=0{\cdot}96a_2$ tooth flank position. The resultant slip distributions, shown in Fig. 13*b*, correspond to the stabilised minor cycles. The slip pattern of the $B_n=0{\cdot}117$ case is similar to that of $B_n=0{\cdot}087$ with a maximum slip occurring at the $z=a_1$ contact end, but with the stick slip interface further away from the $z=a_1$ contact end. With a typical a_2 value of 1·8 mm, the maximum slip value is ~27 μm for $B_n=0{\cdot}117$ and ~11 μm for $B_n=0{\cdot}087$. By contrast, for the design bending moment $B_n=0{\cdot}039$, the slip becomes negligible everywhere, suggesting that the spline teeth remain stuck in this situation. The subsurface stress distributions for the unworn case are discussed in detail in Ref. 13 and are not further discussed here.

Figure 14 shows the major cycle and (stabilised) minor cycle critical plane SWT distributions over the spline surface from the tip of tooth 18 to the adjacent tip of tooth 17, including the spline fillets and root, for the $B_n=0{\cdot}117$ case. It is clear that the critical location for major cycles is the $z=a_1$ axial position in the spline root, $x\approx 2a_2$ with a peak value of ~2·7 MPa, while the critical location for minor cycles is also the $z=a_1$ axial position but at the $x=a_2$ contact edge with a peak value of 1·65 MPa. As discussed previously,[13] these results predict fretting fatigue failure at the $(x, z)=(a_2, a_1)$ contact edge, due to the significantly larger number of minor cycles than major cycles per complete load cycle. Similarly, for the $B_n=0{\cdot}087$ load case, the minor cycle SWT value predominates damage accumulation and failure is again predicted at the $(x, z)=(a_2, a_1)$ contact edge. However, for the $B_n=0{\cdot}039$ load case, plain fatigue failure in the spline root is predicted first due to predominance of the major cycle peak SWT at $z=a_1$ and $x\approx 2a_2$.

Incremental (gross slip) wear predictions

The incremental fretting wear modelling is only applied here to the external spline. A wear coefficient of $5{\cdot}0\times 10^{-8}$ MPa^{-1} is chosen as representative for the present study, based on the data presented in Ref. 14, even though it is well known that the wear coefficient will depend on many factors, including number of fretting cycles, contact pressure and relative slip. The rationale here is to investigate the generic effects of wear-fatigue interaction for fretting fatigue prediction in splined couplings. ΔN is taken as 1000. The incremental wear analyses are carried out for a total of 12 000 cycles, based on the tests described below and elsewhere.[12] Figure 15 shows the predicted distributions of cumulative wear depth versus axial position for different numbers of cycles up to 12 000, for three sample x/a_2 tooth flank positions. It can be seen that the wear is significantly larger at the $x/a_2=1$ transverse contact edge and is smallest at the $x/a_2=0$ contact edge, which is consistent with the pressure distributions of Fig. 10 and

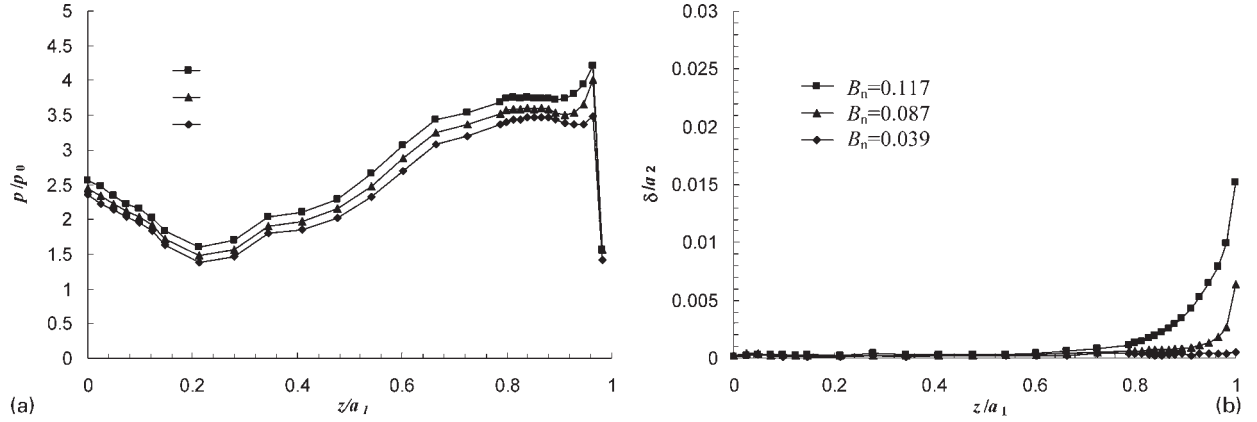

13 Effect of rotating bending moment magnitude on axial distributions of *a* contact pressure and *b* resultant stabilised slip at $x/a_2=0{\cdot}96$ tooth flank position

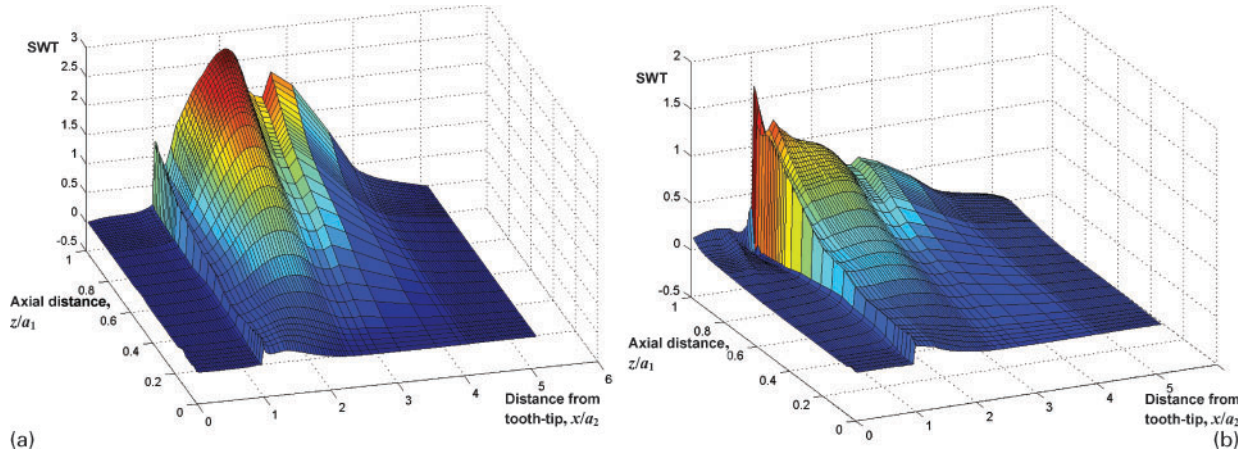

14 Predicted unworn critical plane SWT distributions over spline tooth (from tooth tip on tooth 18 to adjacent tooth tip on tooth 17, including spline fillets and root) for B_n=0·117 case, for *a* major cycle loading (steps 0 to 1) and *b* minor cycle (e.g. steps 4 to 6) loading

the major cycle slip distributions of Fig. 12. A maximum wear depth of ~11 μm is predicted at the x/a_2=1 edge after 12 000 cycles. The axial distribution of wear at the x/a_2=1 edge is concentrated towards the z/a_1=1 end of engagement. Similarly with the axial distribution at the x/a_2=0·5 midtooth position, which reaches a peak value of ~3 μm at $z/a_1 \approx 0{\cdot}8$. Negligible wear is predicted at the x/a_2=0 edge, due to the contact being open here towards the z/a_1=1 end. Figure 16 shows a comparison between the FE determined wear distributions for different tooth flank positions from the cyclic symmetry model and the interpolated wear distributions (using equations (11) and (12)) for the same tooth positions on the 360° model. The significantly greater degree of axial direction mesh refinement on the latter towards the z/a_1=1 end can be seen (this could not be seen in Fig. 4).

Figure 17 shows a set of comparisons, for different tooth flank positions, of the contact pressure distributions versus axial position for the unworn coupling and the worn coupling after 12 000 wear cycles. The key effects are:

(i) at the x/a_2=0 contact edge, the major cycle (step 1) pressure increases or stays about the same in the region $z/a_1 \leqslant 0{\cdot}04$, due to wear, while it reduces in the region $0{\cdot}04 \leqslant z/a_1 \leqslant 0{\cdot}18$

(ii) at the x/a_2=0 contact edge, the minor cycle (step 6: $+B$, T_{max}) distribution in this region shows a mixed effect

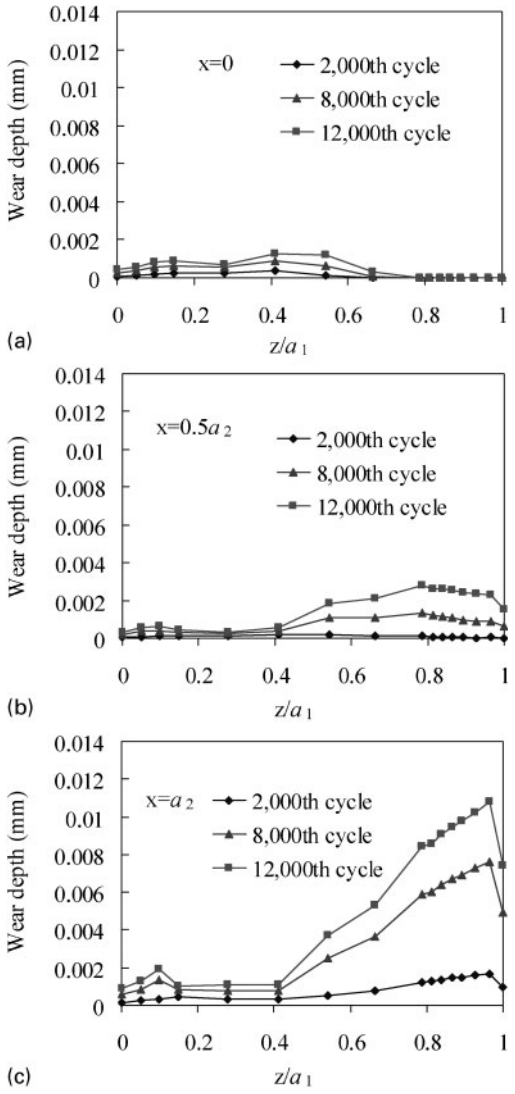

15 Evolution of wear depth distributions versus axial position for different numbers of major cycles for sample tooth flank positions *a* x/a_2=0, *b* x/a_2=0·5 and *c* x/a_2=1, as predicted by one tooth model

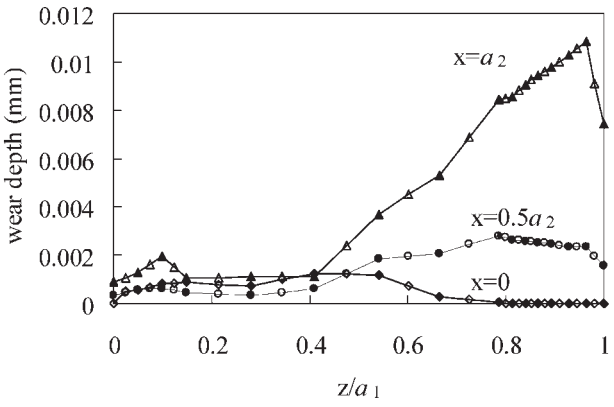

16 Interpolated wear depth data points plotted against axial and radial positions for tooth 18 of 360° spline model at 12 000 cycles: hollow symbols represent interpolated data points; solid symbols represent one-tooth model data points

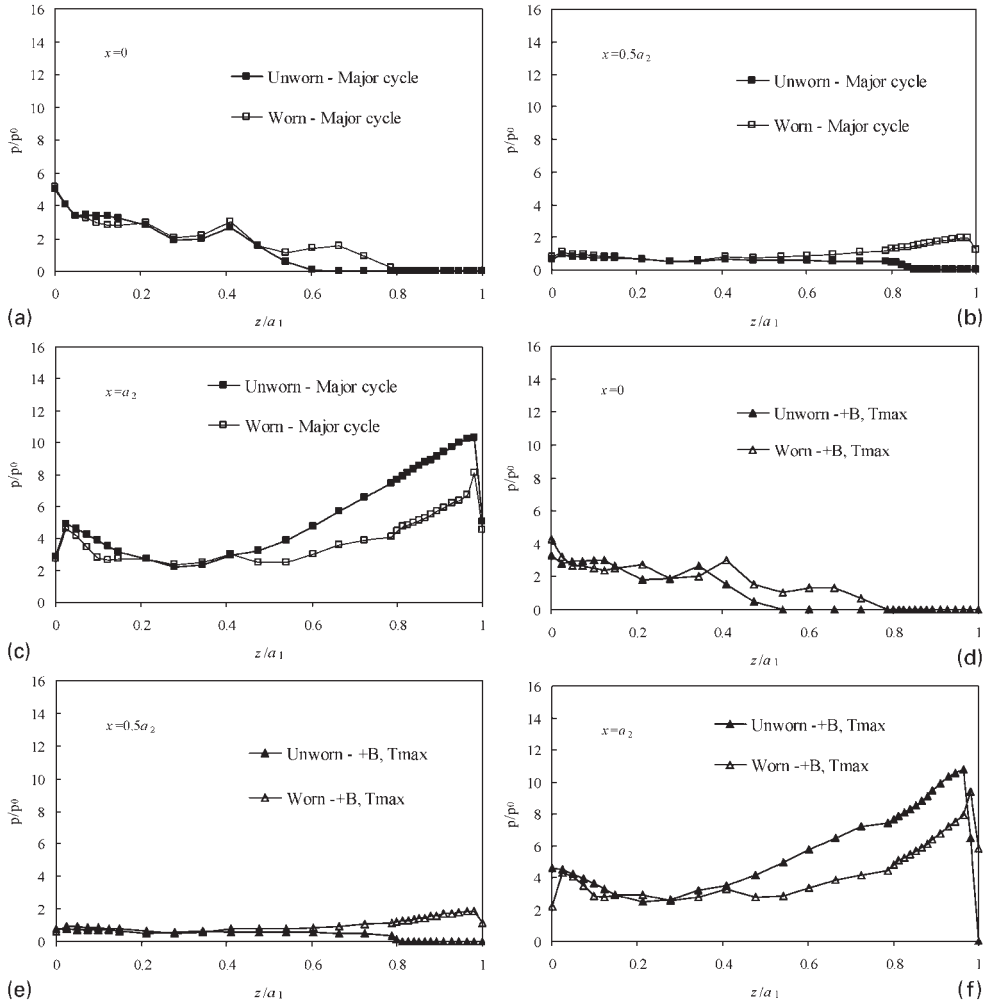

17 Predicted effect of wear (12 000 major cycles) on contact pressure distributions for B_n=0·087 load case, for sample tooth flank positions and loading steps, as follows: *a* step 1, x/a_2=0; *b* step 1, x/a_2=0·52; *c* step 1, x/a_2=1; *d* step 6, x/a_2=0; *e* step 6, x/a_2=0·52; *f* step 6, x/a_2=1

(iii) at the $x/a_2=0$ contact edge, in the region $0{\cdot}4 \leqslant z/a_1 \leqslant 0{\cdot}8$, the major cycle and minor cycle (step 6) pressures increase, reflecting the fact that the contact area has increased here

(iv) at the $x/a_2=0{\cdot}5$ position, the salient effect is a corresponding increase in contact area over the region $0{\cdot}8 \leqslant z/a_1 \leqslant 1$, leading to almost equal pressure distributions for the step 1 and step 6 loads

(v) there is a significant effect at the $x/a_2=1$ contact edge; specifically, there are significant decreases in both step 1 (T_n=0·818, F_n=0·032) and step 6 ($+B$, T_{max}) contact pressures over the region $0{\cdot}4 \leqslant z/a_1 < 1$; for the unworn case, the $z=a_1$ end is out of contact for step 1 but with wear comes into contact under the same load.

Figure 18 shows the predicted critical plane SWT distributions after 12 000 cycles, including the effects of wear, for the B_n=0·087 case. The general effect of major cycle wear is: to reduce the major cycle SWT values, principally at the $x \approx 2a_2$ spline root location and at the $x=a_2$ contact edge; and to reduce the minor cycle SWT values at the $x=a_2$ contact edge and in the spline fillet, but to increase the (significantly lower) values in the contact region, $0{\cdot}5 \leqslant x/a_2 \leqslant 1$.

Partial slip wear predictions

The slip patterns associated with the major cycle loading, for which incremental wear calculations have been carried out above, correspond to gross slip in fretting wear and fatigue terminology. Essentially, this means that there is no stick zone on the contact surface, i.e. all points have non-zero relative slip. But as discussed above, the predicted effect of gross slip wear in fretting fatigue is quite different to that of partial slip, both in terms of effect on life and cracking location. Specifically, in simple Hertzian fretting tests, gross slip wear leads to increased life relative to no-wear calculations, typically with the same failure location, while partial slip wear leads to similar life but the failure location can move to within the slip zone depending on the relative rates of accumulation of fatigue damage and wear, e.g. Ref. 10. Furthermore, as shown in Fig. 13*b*, the minor cycle loading leads to a partial slip situation, with the slip concentrated towards the $z=a_1$ end. Given that an incremental minor (partial slip) wear simulation is prohibitive, due to: the large number of minor cycles; the large size of the 360° model; and the computational intensity of incremental wear simulations in the spline, the following procedure is adopted here to investigate the effect of partial slip wear:

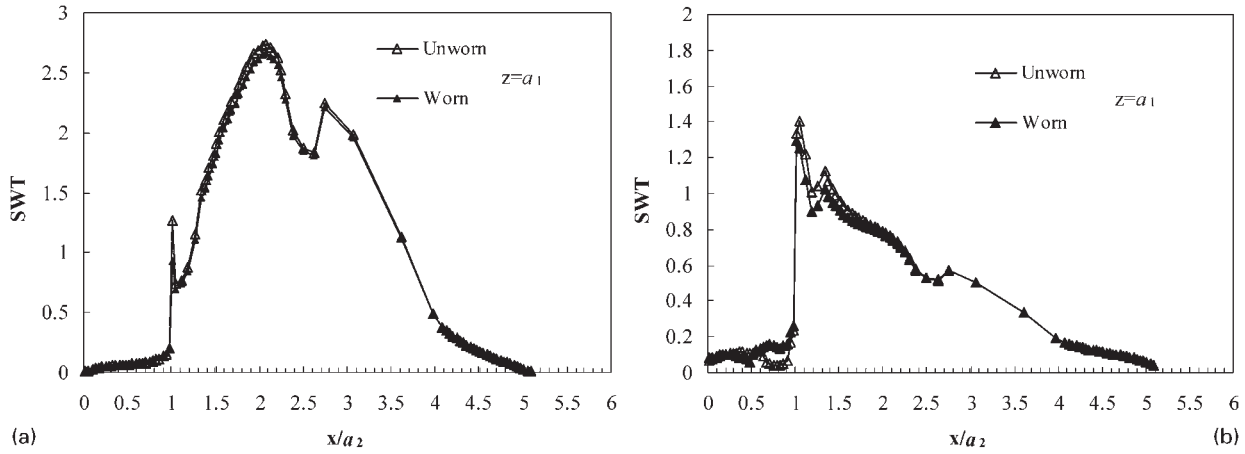

18 Predicted effect of incremental (major cycle) wear (12 000 cycles) on critical plane SWT distributions at $z/a_1=1$ axial position for *a* major cycle (steps 0 to 1) loading and *b* minor cycle (e.g. steps 4 to 6) loading for $B_n=0{\cdot}087$ loading

(i) step 1: assume a partial slip wear pattern, based on a measured wear depth at the $z=a_1$ end (e.g. Ref. 14) and assume that the variation elsewhere along the z direction scales with relative slip. For simplicity, assume this is independent of tooth flank position, i.e. is independent of x

(ii) step 2: apply this to the 360° model using the interpolation technique described above

(iii) step 3: run 360° model analyses according to the loading steps of Fig. 5 and post-process to determine critical plane distributions of SWT under major cycles and minor cycles.

As an example for the $B_n=0{\cdot}117$ case, a measured wear depth of 6 μm is taken[14] with an assumed wear depth distribution shown in Fig. 19, to examine the effect of partial slip on fretting fatigue life. Note that this wear is attributed predominantly to minor cycle fretting, as discussed in Ref. 14, based on predicted slip COF relationships and measured COF–N relationships. Figure 20 shows the effect of this wear on the axial distributions of contact pressure for major and minor load steps. The key predicted effect of the partial slip wear is the movement of the peak pressure position away from $z/a_1\approx1$ to $z/a_1\approx0{\cdot}85$. Figure 21 shows the resulting predicted major and minor cycle critical plane SWT distributions and Fig. 22 compares the minor cycle distributions for the unworn and worn cases at two key axial positions. These results illustrate the following key points:

(i) a decrease in the major and minor cycle SWT values at $z=a_1$ due to the partial slip wear

(ii) an increase in the values near the stick slip interface, leading to a shift in axial location of the peaks to $z/a_1\approx0{\cdot}8$ (cf. Fig. 14*a*).

Life predictions

Table 3 shows the calculated fatigue lives and failure locations for three different rotating bending moment B_n levels of 0·039, 0·087 and 0·117, using the assumptions of no wear, gross slip wear and partial slip wear, along with equations (8)–(10). In the case of the latter assumption, results are only presented for the $B_n=0{\cdot}117$ case. For comparison purposes, Table 4 presents the test data corresponding to the same three bending moment levels. The following observations can be made from these results:

(i) the no-wear assumption predicts a trend of decreasing life with increasing bending moment, which is consistent with the test data. In the $0{\cdot}039B_n$ case, torque dominated plain fatigue failure is predicted in the spline fillet/root region; the corresponding test is stopped before this number of cycles. For the higher bending loads, fretting fatigue failure is predicted at the (x, z)=(a_2, a_1) contact edge. In the tests, however, the cracking was observed under the contact,

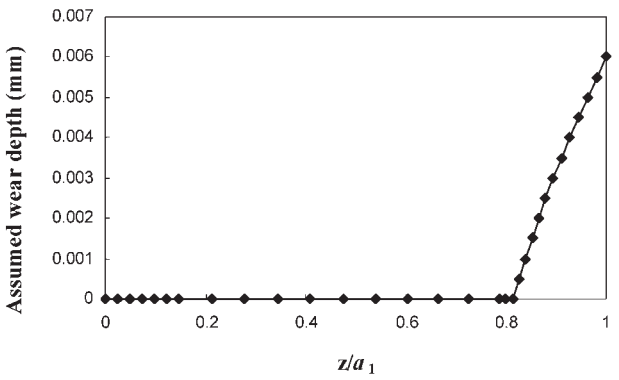

19 Assumed partial slip wear depth distribution for $B_n=0{\cdot}117$ load case, corresponding to 1490 (major) wear cycles

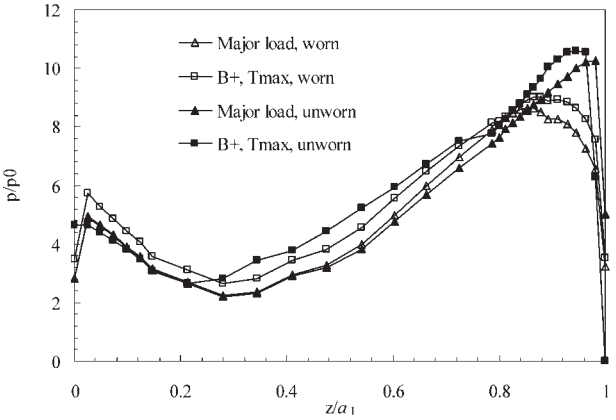

20 Predicted effect of partial slip wear on contact pressure distributions versus axial position for tooth flank of $x/a_2=1$ and for $B_n=0{\cdot}117$ load case

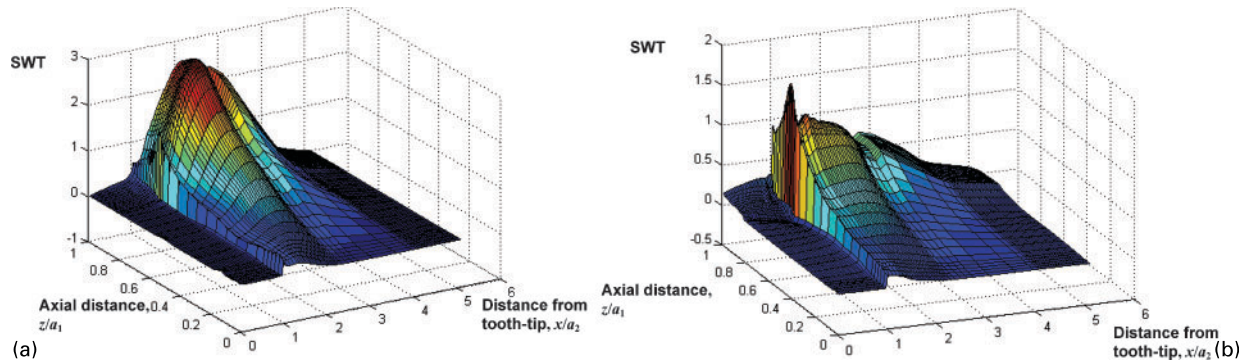

21 Predicted *a* major and *b* minor cycle critical plane SWT distributions for partial slip wear for B_n=0·117 load case

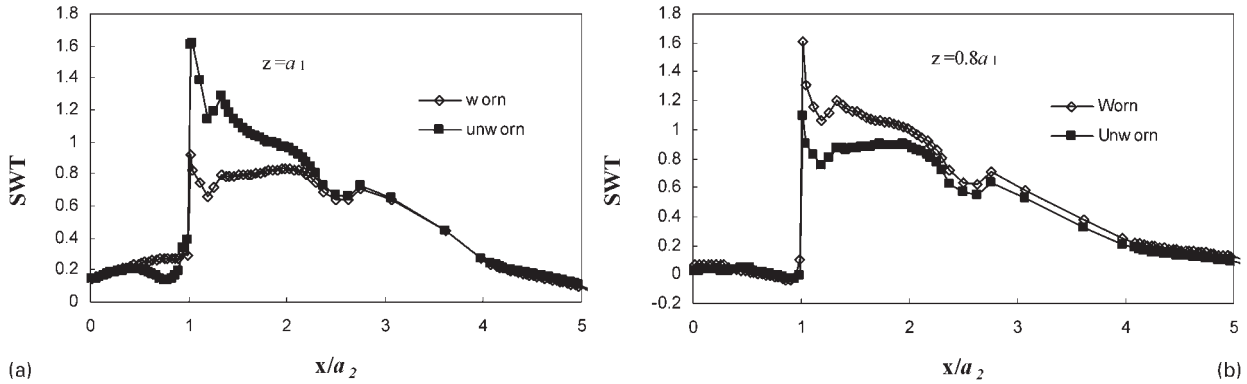

22 Predicted effect of partial slip wear on minor cycle critical plane SWT distributions for B_n=0·117 load case at *a* z/a_1=1 and *b* z/a_1=0·8

away from the contact edge, both axially and radially

(ii) the assumption of the gross slip predicts an increase in life relative to the no-wear assumption, due to the general reduction in critical plane SWT values caused primarily by stress redistribution associated with the wear induced increased contact patch. In the B_n=0·087 and B_n=0·117 cases, the predicted lives thus diverge further from the test lives. For the B_n=0·117 case, the predicted failure location remains at the (x, z)=(a_2, a_1) contact edge. This is consistent with the predictions of Madge *et al.*[10,11] and test data for simpler fretting fatigue test geometries. However, in these simpler cases, where either gross or partial slip conditions pertain, the wear induced increased life improved the correlation of predictions with test data, relative to the no-wear assumption. In the present spline analyses, major cycle loads are predicted to give gross slip conditions, but the superimposed minor cycle loads are predicted to give partial slip conditions, so that the wear fatigue interaction effects are significantly more complex. For the B_n=0·087 case, the gross slip wear assumption also reduces the contact edge fretting fatigue damage so much that torque dominated plain fatigue failure is predicted to occur first in the spline fillet root. This is not consistent with the test observations for this load case

Table 3 Comparison of predicted lives (number of minor cycles to failure) as obtained using different wear assumptions, for different values of rotating bending moment

Wear assumption	Parameter	B_n=0·039	B_n=0·087	B_n=0·117
No wear	Life	$2·2 \times 10^7$	$1·54 \times 10^7$	$2·15 \times 10^6$
	Failure location (x/a_2, z/a_1)	(2·03,1·02)	(1·0, 1·02)	(1·0, 1·02)
Gross slip (major cycle) wear	Life	$2·94 \times 10^7$	$2·64 \times 10^7$	$2·4 \times 10^6$
	Failure location (x/a_2, z/a_1)	(2·03,1·02)	(2·03, 1·02)	(1·0, 1·02)
Partial slip (minor cycle) wear	Life	N/A	N/A	$1·65 \times 10^6$
	Failure location (x/a_2, z/a_1)	N/A	N/A	(1·0, 0·8)

Table 4 Summary of spline test conditions and associated results of fretting damage[12]

Parameter	B_n=0·039	B_n=0·087	B_n=0·117
Life (major cycles)	>35 000	12,021	1490
Life (minor cycles)	$>1·75 \times 10^7$	$6·01 \times 10^6$	$7·45 \times 10^5$
Crack initiation location (x/a_2, z/a_1)	–	(0–1, 0·7–0·94)	(0–1, 0·7–0·87)

(iii) the use of the partial slip wear assumption for the $B_n=0{\cdot}117$ case, which is argued to be a minor cycle dominated damage case (by virtue of the small number of major cycles tested), leads to an improved life prediction vis-à-vis the test life and relative to both the gross slip wear assumption and the no-wear assumption. Furthermore, the predicted axial location of failure has changed from the contact edge to the stick slip interface, which is consistent with the test data. In the tests, the crack initiation appears to initiate from within the $0<x/a_2<1$ region, as opposed to the predicted location of $x=a_2$. The assumption of uniform wear in the x direction in the assumed partial slip wear distribution of Fig. 19 is a likely explanation for this inconsistency.

Note that in the gross slip wear cases, a linear variation of SWT with number of cycles, based on the $N=0$ and $N=12\,000$ results, is employed to extrapolate to larger numbers of cycles for cumulative damage predictions using SWT. Similarly, in the partial slip wear case, a linear variation of SWT based on the $N=0$ and $N=1490$ results facilitates extrapolation to larger numbers of cycles for cumulative damage prediction.

Conclusions

An FE based study of the effects of wear on fretting fatigue and plain fatigue life and failure location in splines is presented. A number of simplifying assumptions have been necessary in order to achieve this, including the following.

1. Only external spline teeth are assumed to wear.
2. The wear coefficient is assumed to be constant.
3. The COF is assumed to be constant.
4. Identical (initial) spline teeth are assumed.
5. A total life method is employed, which thereby effectively ignores stress gradient effects and short crack growth.
6. Miner's rule is assumed for cumulative damage.
7. No additional surface damage effects are incorporated other than material removal.

The combined (major cycle) low frequency torque and axial load and higher frequency (minor cycle) rotating bending moment and fluctuating torque analysis predicts that major cycles lead to gross slip and minor cycles lead to partial slip. It is shown that the effect of (incremental) gross slip wear is to increase the contact area, reduce the contact pressure and reduce the predicted fretting fatigue damage. It is shown that the effect of (minor cycle) partial slip wear is to increase the predicted fretting fatigue damage, to move the predicted failure location towards the stick-slip interface and thus to give an improved correlation with the test results. A robust wear fatigue life prediction methodology for spline couplings, for the types of loads considered here, requires the ability the incrementally simulate minor cycle (partial slip) wear, as well as major cycle (gross slip) wear.

Future work will address this computationally intensive problem. However, the key finding of this paper is the importance of simulating wear induced geometry evolution for accurate life and failure location predictions.

Acknowledgements

The authors wish to thank Rolls-Royce plc, Aerospace Group, for their financial support of the research, which was carried out at the University Technology Centre in Gas Turbine Transmission Systems at the University of Nottingham. The views expressed in this paper are those of the authors and not necessarily those of Rolls-Royce plc, Aerospace Group. The authors would also like to honour the memory of our colleague Dr Ian R McColl, who passed away on 30 November, 2005.

References

1. O. Vingsbo and D. Soderberg: *Wear*, 1988, **126**, (2), 131–147.
2. M. P. Szolwinski and T. N. Farris: *Wear*, **198**, 1996, 93–107.
3. C. D. Lykins, S. Mall and V. Jain: *Int. J. Fatig.*, 2000, **22**, 703–716.
4. J. A. Araujo and D. Nowell: *Int. J. Fatig.* 2002, **24**, 763–775.
5. W. S. Sum, E. J. Williams and S. B. Leen: *Int. J. Fatig.*, 2005, **27**, (4), 403–416.
6. O. Jin and S. Mall: *Wear*, 2004, **256**, 671–684.
7. C. Ruiz, P. H. B. Boddington and K. C.Chen: *Experim. Mech.*, 1984, **24**, (3), 208–217.
8. I. R. McColl, J. Ding and S. B. Leen: *Wear*, 2004, **256**, 1114–1127.
9. J. Ding, S. B. Leen and I. R. McColl: *Int. J. Fatig.*, 2004, **26**, 521–531.
10. J. J. Madge, S. B. Leen and P. H. Shipway: *Wear*, 2007, **263**, 542–551.
11. J. J. Madge, S. B. Leen, I. R. McColl and P. H. Shipway: *Wear*, 2007, **262**, 1159–1170.
12. S. B. Leen, T. H. Hyde, C. H. H. Ratsimba, E. J. Williams and I. R. McColl: *J. Strain Anal. Eng. Design*, 2002, **37**, (6), 565–583.
13. J. Ding, W. S. Sum, R. Sabesan, S. B. Leen, I. R. McColl and E. J. Williams: *Int. J. Fatig.*, 2007, **29**, 1229–1244.
14. C. H. H. Ratsimba, I. R. McColl, E. J. Williams, S. B. Leen and H. P. Soh: *Wear*, 2004, **257**, 1193–1206.
15. W. Sum, S. B. Leen, E. J. Williams, S. Rajaratnam and I. R. McColl: *J Strain Anal.*, 2005, **40**, (7), 655–673.
16. J. Ding: 'Modelling of fretting wear', PhD thesis, University of Nottingham, Nottingham, UK, 2003.
17. S. Medina and A. V. Olver: *J. Eng. Tribol.*, 2002, **216**, 269–279.
18. J. Ding, I. R. McColl and S. B. Leen: *Wear*, 2007, **262**, 1205–1216.
19. M. A. Miner: *Trans. ASME*, 1945, **67**, A159–A164.
20. P. Lancaster and K. Salkauskas: 'Curve and surface fitting: an introduction'; 1986, New York, Academic Press.